Article

Frequency reproducibility of solid-state thorium-229 nuclear clocks

https://doi.org/10.1038/s41586-025-09999-5

Received: 19 June 2025

Accepted: 3 December 2025

Published online: 28 January 2026

Check for updates

Tian Ooi[1], Jack F. Doyle[1], Chuankun Zhang[1], Jacob S. Higgins[1], Jun Ye[1]✉, Kjeld Beeks[2], Tomas Sikorsky[2] & Thorsten Schumm[2]

Solid-state thorium-229 (^{229}Th) nuclear clocks[1–5] are set to provide new opportunities for precision metrology and fundamental physics[6–8]. Taking advantage of inherent low sensitivity of a nuclear transition to its environment[9], orders of magnitude more emitters can be hosted in a solid-state crystal compared with current optical lattice atomic clocks[10]. Furthermore, solid-state systems needing only simple thermal control[11] are key to the development of field-deployable compact clocks. Here we explore and characterize the frequency reproducibility of the ^{229}Th:CaF_2 nuclear clock transition, a key performance metric for all clocks. We measure the transition linewidth and centre frequency as a function of the doping concentration, temperature and time. We report the concentration-dependent inhomogeneous linewidth of the nuclear transition, limited by the intrinsic host crystal[12] properties. We determine an optimal working temperature for the ^{229}Th:CaF_2 nuclear clock at 196(5) K, at which the first-order thermal sensitivity vanishes. This would enable in situ temperature co-sensing using different quadrupole-split lines, reducing the temperature-induced systematic shift below the 10^{-18} fractional frequency uncertainty level. At 195 K, the reproducibility of the nuclear transition frequency is 220 Hz (fractionally 1.1×10^{-13}) for two differently doped ^{229}Th:CaF_2 crystals over 7 months. These results form the foundation for understanding, controlling and harnessing the coherent nuclear excitation of ^{229}Th in solid-state hosts and for their applications in constraining temporal variations of fundamental constants.

Optical atomic clocks are the most precise timekeepers of the world and are poised to answer a wealth of fundamental questions, including searches for new physics beyond the Standard Model[13]. Taking advantage of electronic transitions in atoms with long coherence times, optical clocks have achieved systematic uncertainties below 10^{-18} (refs. 10,14) with measurement precision approaching 10^{-21} (ref. 15). Optical lattice clocks achieve this superior precision by scaling the number of quantum absorbers to 10^5, greatly reducing the quantum projection noise limit.

Nuclear clocks, based on transitions within nuclei as a frequency reference[3], can further scale the number of absorbers to more than 10^{15} by using solid-state hosts, potentially opening up new regimes of clock stability[9,16]. The thorium-229 (^{229}Th) isotope has a uniquely low-energy metastable nuclear isomeric state (^{229m}Th) around 8.4 eV above the ground state, corresponding to a wavelength of around 148.38 nm, accessible by tabletop lasers. This ^{229m}Th transition has been proposed[17,18] for a next-generation optical clock[5,19,20]. The relative insensitivity of nuclear energy states to external perturbations compared with electronic states makes this type of clock inherently more stable and suitable for embedding in a solid-state crystal[18].

Following a series of indirect and direct observations of the ^{229}Th nuclear transition energy[21–27], the first resonant excitation was achieved in a ^{229}Th-doped calcium fluoride (^{229}Th:CaF_2) crystal[1], followed by excitation in a ^{229}Th:$LiSrAlF_6$ crystal[2]. The first frequency-based measurement[3] was achieved using a vacuum ultraviolet (VUV) frequency comb[28] linked to the JILA ^{87}Sr optical atomic clock. This work measured the transition frequency at kHz-level precision and resolved the nuclear electric quadrupole splitting in ^{229}Th:CaF_2 crystals. The precise measurement of the electric quadrupole ratio between the ground and excited states allowed the determination of the volume ratio of these two nuclear states and a new estimate of the transition sensitivity to variations of the fine structure constant α (refs. 6,7). The ^{229}Th resonant excitation has also been observed in $^{229}ThF_4$ and $^{229}ThO_2$ thin films[4,29], an important step towards portable nuclear clocks that can be prepared inexpensively with minimal starting material.

Developing a new clock platform requires a thorough understanding of systematic effects that can perturb transition frequencies. These perturbations can arise from external electric and magnetic fields or the host environment. Building on our first characterization of temperature-induced frequency shifts[11], here we report the frequency reproducibility of the nuclear transition in ^{229}Th:CaF_2 across a large range of doping concentrations, temperature and temporal duration. We find that the crystal-limited transition linewidths do not change over a large temperature range, but increase with thorium concentration because of dopant-induced inhomogeneous broadening. We report a zero-shift temperature, at which the local slope of the transition

[1]JILA, NIST and University of Colorado, Department of Physics, University of Colorado, Boulder, CO, USA. [2]Vienna Center for Quantum Science and Technology, Atominstitut, TU Wien, Vienna, Austria. ✉e-mail: ye@jila.colorado.edu

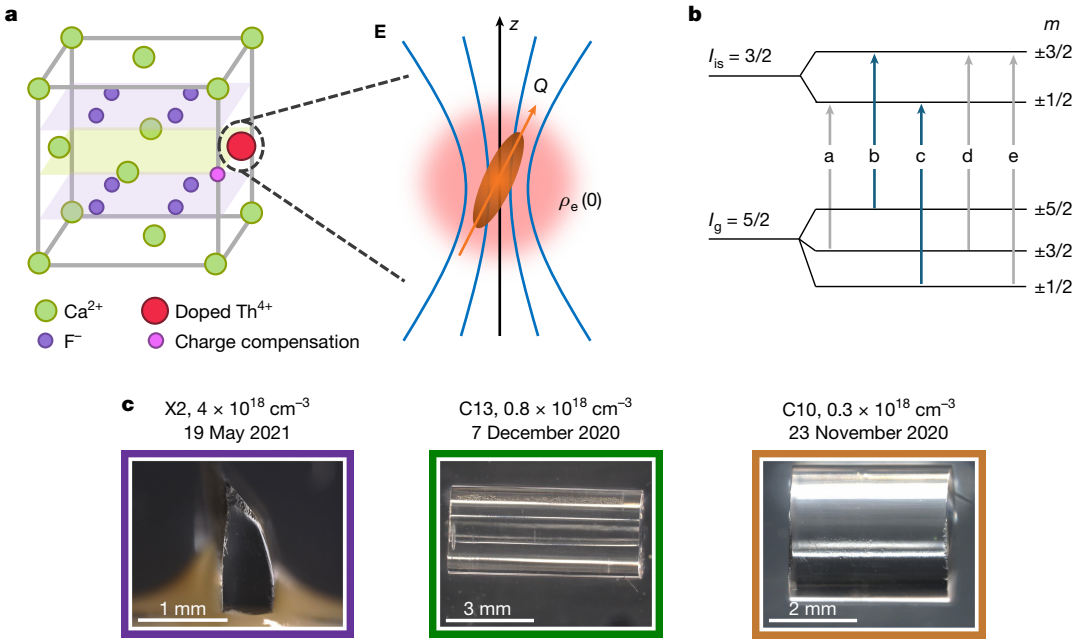

Fig. 1 | Context for the characterization of nuclear clock reproducibility. **a**, A ^{229}Th nucleus hosted inside a CaF_2 crystal experiences a local EFG $\nabla\mathbf{E}$ (blue) and a local charge density $\rho_e(0)$ (red). The ^{229}Th nuclear electric quadrupole moment Q (orange) interacts with $\nabla\mathbf{E}$, leading to split energy levels. **b**, Level diagram with electric quadrupole splitting. The ground (spin $I_g = 5/2$) and excited isomeric state (spin $I_{is} = 3/2$) are split into 3 and 2 sub-levels, respectively. I denotes nuclear angular momentum and m is the projection of I along the z-axis. Five allowed transitions are labelled as lines a–e. Line b and c (highlighted in blue) are characterized in this work, as their properties are desirable for construction of a clock. **c**, Microscope images of the three crystals used in this work, with their corresponding fabrication date and ^{229}Th doping concentration labelled. The coloured border around the image will be used throughout this paper to indicate the corresponding crystal in all further plots.

frequency compared with temperature curve vanishes. The different temperature sensitivities of two transition lines can be used for a co-thermometry stabilization scheme in future clock operation. Finally, we report that the transition frequency remains stable at the kHz level over the course of many months and across different crystals, with two of the crystals demonstrating sub-kHz reproducibility with a standard error of 220 Hz at the zero-shift temperature. This demonstrates the power of this platform as a frequency standard, in which frequency reproducibility is paramount.

State-resolved nuclear spectroscopy

We use ^{229}Th:CaF_2 crystals grown with the vertical gradient freeze method at TU Wien[12,30]. The ^{229}Th atom substitutes with Ca^{2+} as $^{229}Th^{4+}$, creating a local defect that requires charge compensation[31] (Fig. 1a). The microscopic charge compensation mechanism is an area of active research[32,33]. A recent work[34] identifies four different defect sites in ^{229}Th:CaF_2 and proposes a cluster of two $^{229}Th^{4+}$ located at neighbouring Ca^{2+} sites with a non-local charge compensation for the quadrupole structure studied in this work. As the CaF_2 bandgap is larger than the 8.4 eV nuclear transition, we expect radiative decay to dominate over internal conversion. However, electronic defect states within the bandgap may introduce weak coupling to the ^{229}Th nuclei that lead to quenching effects[29,35]. Although the nuclear transition has reduced environmental sensitivity, a temperature-dependent frequency shift is observed, arising mainly from two effects in the host crystal[11]. First, the ^{229}Th nuclear ground and excited states have different mean charge radii[6,22], leading to an electric monopole shift dependent on the local electron charge density at the nucleus $\rho_e(0)$. Second, the nuclear spin and quadrupole moment also change between ground and excited states, leading to an electric quadrupole shift dependent on the local electric field gradient (EFG) $\nabla\mathbf{E}$. Although cubic crystals such as CaF_2 have a vanishing EFG at the Ca substitutional position[36], a non-zero EFG in ^{229}Th:CaF_2 arises from the local microscopic defect configuration around the ^{229}Th dopant and sets the quantization axis (z-axis in Fig. 1a) of the nuclear spin orientation. The electric quadrupole interaction Hamiltonian[37] $H_{E2} = \frac{QV_{zz}}{4I(2I-1)}[3I_z^2 - \mathbf{I}^2 + \eta(I_x^2 - I_y^2)]$ also leads to the splitting of the nuclear states and five asymptotically allowed transitions[6] given by the selection rule $\Delta m = 0, \pm 1$ (Fig. 1b). Here, Q is the spectroscopic nuclear electric quadrupole moment, I is the nuclear angular momentum and m is the projection of I along the z-axis. In the diagonal EFG matrix V_{ij}, V_{zz} describes the z-component and $\eta = (V_{xx} - V_{yy})/V_{zz}$ describes the field asymmetry. As the crystal temperature varies, changes in phonon occupation and interatomic distances affect $\rho_e(0)$ and $\nabla\mathbf{E}$, causing nuclear transition frequency shifts. In previous work, we measured the state-resolved transition line frequencies[3] and characterized their temperature dependence[11] in a ^{229}Th:CaF_2 crystal[12], named X2.

We now focus on the lines with the smallest ($m = \pm 5/2 \rightarrow m = \pm 3/2$, line b) and largest ($m = \pm 1/2 \rightarrow m = \pm 1/2$, line c) temperature sensitivity (Fig. 1b). We extend the nuclear spectroscopy to three different CaF_2 crystals (X2, C13 and C10), with their ^{229}Th concentration and fabrication date listed in Fig. 1c. X2 is glued with Epotek H77 to a MgF_2 disc, which is in turn clamped to a copper mount, whereas C10 and C13 are tied with wire to a copper mount, using indium foil for improved thermal contact. The temperature is measured using a sensor mounted to the crystal holder and stabilized by feedback onto a heater on the copper thermal link connecting a liquid nitrogen dewar and the crystal mount[11]. The estimated steady-state temperature difference caused by the laser between the crystal and mount is <200 mK. After changing temperatures, we wait for a few hours to ensure thermal equilibrium. During the scans, the crystal temperature does not deviate by more than 0.1 K.

A typical line scan is shown in Fig. 2a (inset), corresponding to line b of crystal C10 at 175 K. For each point of the scan (open circles), we irradiate the target with our VUV frequency comb[28] for 400 s. We then turn off the laser and count VUV photons emitted from the crystal over a 200 s detection window. We take the average count rate over the detection window after correcting for known systematics such as fluctuations in laser intensity and residual excitation from previous

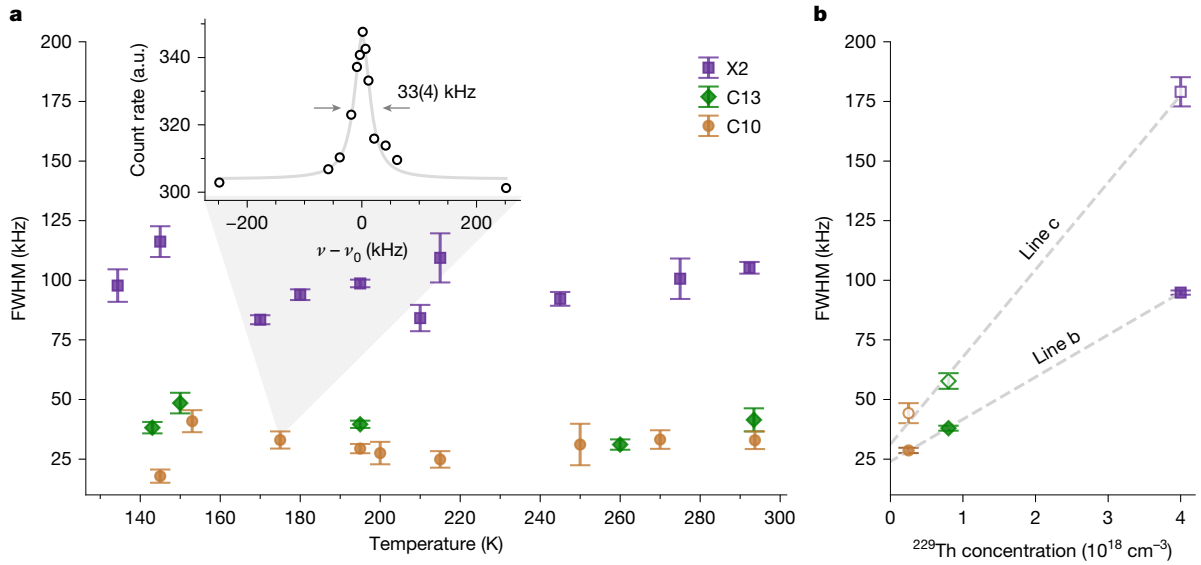

Fig. 2 | Characterization of the nuclear clock transition linewidth in CaF_2 host. a, Observed nuclear transition FWHM linewidth of line b as a function of temperature across three different crystals (X2, C13 and C10). Error bars are derived from the FWHM uncertainty of the Lorentzian fit. When multiple sets of data are taken at the same temperature within 1 K, the FWHM is represented by the weighted average. The inset shows a typical line scan with data fitted to a Lorentzian line shape (a.u., arbitrary units). The fit yields a centre frequency of $\nu_0 = 2{,}020{,}407{,}298{,}706.6(8)$ kHz and a linewidth of 33(4) kHz. For each scan, we correct the count rate and frequency by accounting for known line-skewing effects (Methods). **b**, Observed nuclear transition linewidth scaling in different crystals for both lines b and c. Lower doping concentration leads to a narrower transition linewidth. Linear fits to the data are presented as a visual guide. Line c shows a wider linewidth compared with line b for all crystals used in this experiment.

points (Methods). Fitting a Lorentzian lineshape (grey line) to the data, we extract the centre frequency, full-width-at-half-maximum (FWHM) linewidth and their uncertainties.

Since May 2024, we have accumulated a database of 73 line scans at temperatures ranging from 134 K to 294 K across the three crystals. In the following, we characterize the reproducibility of the nuclear clock transition frequency and linewidth as a function of temperature, ^{229}Th doping concentration and time.

Linewidth characterization

The observed isomeric state life time of 641(4) s (ref. 3) would correspond to a superior transition quality factor exceeding 10^{19}. However, in previous work, we observed linewidths between 200 kHz and 300 kHz in X2 (ref. 3) (Methods). It is thus crucial to explore the origin of linewidth broadening in the crystal. We begin by studying the relationship between line b linewidth and temperature, recorded in Fig. 2a for C10, C13 and X2 (orange circle, green diamond and purple square, respectively). When multiple linescans are taken for a crystal at the same temperature (within 1 K), the linewidth is represented by their weighted average. Across the measured temperatures, no temperature dependence of the transition linewidth is observed.

By contrast, we observe clear linewidth dependence on the ^{229}Th doping concentration and the individual transition line. Figure 2b shows the FWHM linewidth as a function of ^{229}Th doping concentration for all three crystals. Filled markers correspond to line b, whereas unfilled markers correspond to line c. Each marker represents the weighted average of data over all temperatures. Linear fits to line b yield a slope of 17.7(3) kHz/10^{18} cm^{-3} and an intercept of 24.0(9) kHz, and fits to line c yield a slope of 37(2) kHz/10^{18} cm^{-3} and an intercept of 31(3) kHz. The weighted average of the measured linewidths of C10 line b is 29(1) kHz, and the narrowest feature we observe in C10 has an FWHM of 18(3) kHz.

Although we have not directly measured the linewidth of our VUV comb, spectral analysis suggests that it is of the order of 1 kHz (ref. 28). Our nuclear spectroscopy measurements provide a further insight: the measured linear relationship of linewidth to near zero concentration suggests that the comb linewidth is below the observed values reported here. Further details on linewidth analysis can be found in the Methods.

Zero-shift temperature and co-thermometry

We measure the nuclear transition centre frequency at various crystal temperatures ranging from 134 K to 293 K. As shown in Fig. 3, the transition frequencies have good agreement among the three different crystals at all measured temperatures. For both lines b and c, the centre frequencies ν_b and ν_c are plotted as a function of temperature. Points from the same crystal taken within 1 K temperature are represented by their weighted average. The grey lines show the fit of a quadratic function to the C10 and C13 data, with the fit residuals plotted in the bottom panels (see Extended Data Table 1 for fitted parameters).

Line b has the lowest temperature sensitivity across the four observed transition lines in ref. 11, changing by only 80 kHz over the measured temperature range. This arises from a partial cancellation of the electric monopole (E1) and electric quadrupole (E2) shift as lattice vibrations and lattice constant change with temperature. We observe a local minimum of line b frequency at $T_0 = 196(5)$ K (Fig. 3a), in which the first-order dependence of the transition frequency on temperature vanishes. By using the unsplit frequency (calculated by taking a proper average of the quadrupole-split frequencies[11]), we can separate the E1 and E2 shift and show that the E2 shift follows the more commonly observed $T^{3/2}$ behaviour[38] (Methods). Theoretical models have been developed for both shift effects[39,40]. Quantitative calculations for ^{229}Th:CaF_2 using density functional theory are in progress; however, they will be highly sensitive to the local electronic levels determined by the microscopic defect structure. The X2 data show a larger frequency spread compared with C10 and C13. We speculate that this may arise from stress-induced frequency shifts from the mounting glue contracting as the temperature decreases. The smaller crystal size may also make X2 more susceptible to local laser heating effects.

By contrast, line c frequency has the strongest dependence on temperature and varies by 2.5 MHz over the same range (Fig. 3b).

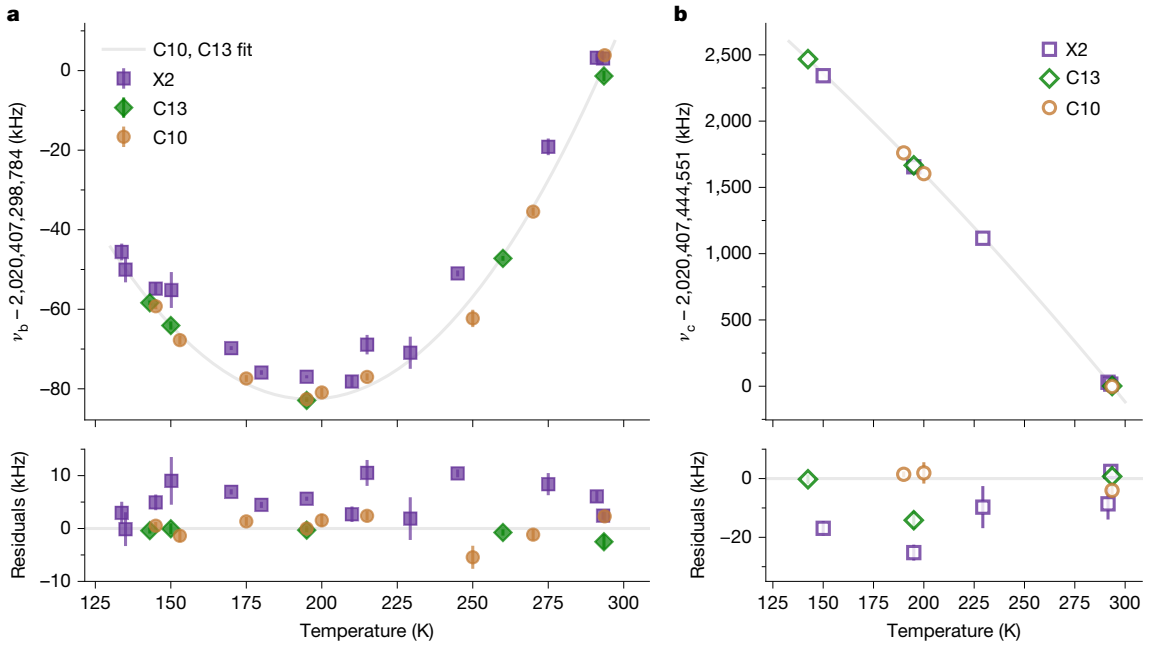

Fig. 3 | Temperature reproducibility of the nuclear clock. For both plots, the optical frequency of the nuclear clock transition is plotted against temperature, with error bars derived from the Lorentzian fit uncertainty. Multiple linescans taken at the same temperature within 1 K are represented by their weighted average. A quadratic fit to the C10 and C13 data is shown in light grey. Residuals from the quadratic fit are shown in the bottom panel. **a**, Temperature dependence of line b frequency ν_b. The minimum in this graph at 196(5) K indicates a temperature at which ν_b has no first-order frequency dependence on temperature, an ideal operating point for a clock. **b**, Temperature dependence of line c frequency ν_c, the most sensitive to temperature variation. This frequency can be used to precisely monitor the crystal temperature.

Leveraging the greater temperature sensitivity, a co-thermometry setup can be implemented using the line c frequency to directly measure the crystal temperature in situ. Assuming we can measure ν_c to 1 kHz uncertainty, this corresponds to a temperature uncertainty of 0.06 K at T_0. Thus, guided by line c, the crystal temperature can be set to $T = T_0 \pm 0.06$ K. Then, a 1 mK temperature reproducibility by active stabilization would result in a line b frequency reproducibility of 1 mHz, corresponding to a fractional frequency reproducibility of 5×10^{-19}.

Frequency reproducibility over time and crystals

Over a time period of 1 year, the nuclear transition frequency has shown good reproducibility at the kHz level among the three crystals. All measurements are referenced to the Sr clock laser[10,41], which enables consistent frequency comparisons over many months. Known systematic shifts, including the silicon reference cavity drift[42], are accounted for (Methods).

Figure 4a shows the frequency of line b at 195.0(1) K, near the zero-shift temperature T_0, for C10 and C13 over a 7-month period. The weighted mean is $\nu_{b,195K}$ = 2,020,407,298,701.18 kHz, with a standard error of 0.22 kHz (light grey band) and reduced chi-squared $\tilde{\chi}^2 = 0.4$. Error bars represent the 1σ uncertainty from the Lorentzian fit.

In comparison, Fig. 4b shows the centre frequency of line b at 293(1) K in all three crystals over a 1-year time period. The weighted average is $\nu_{b,293K}$ = 2,020,407,298,787 kHz with a standard error of 2 kHz. For some room temperature data, the crystal temperature is not actively stabilized, which could account for some frequency spread.

To visualize the temporal consistency of the line b data across all temperatures, we subtract the measured temperature-dependent shifts using the fit shown in Fig. 3. The result shown in Fig. 4c contains similar data as the residuals shown in Fig. 3a (bottom) but is plotted against date instead of temperature. Error bars represent the uncertainty from the Lorentzian fit and also the error from subtracting the temperature shift. Line scans from earlier dates have fewer points near the peak compared with the later dates, leading to a larger Lorentzian fit uncertainty. Across the three crystals over the 1-year period, the centre frequencies show good agreement at the kHz level.

Inhomogeneous broadening mechanism

Initial estimates for ^{229}Th:CaF_2 (ref. 9) predicted that the spectroscopic linewidth would be of the order of 1 kHz, dominated by the inhomogeneous broadening from the magnetic dipole interaction. Other mechanisms such as nuclear electric quadrupole interaction with phonons and second-order Doppler broadening were estimated to be hundreds of Hz. However, we observe much larger linewidths of 10s to 100s of kHz, suggesting a broadening mechanism different from previous considerations[9,16].

We suggest that the observed linewidth is dominated by crystal inhomogeneity due to microstrain from neighbouring ^{229}Th defects that distort the local EFG. The density of thorium in the studied crystals (0.3×10^{18} cm^{-3} to 4×10^{18} cm^{-3}) corresponds to an average distance of d = 60–150 Å between ^{229}Th dopants. Although this distance is large compared with the CaF_2 lattice constant of 5.5 Å, the ^{229}Th site distorts the crystal lattice, creating a long-range microstrain extending over many lattice spacings[43]. As each defect is randomly dispersed throughout the crystal, we expect each ^{229}Th nucleus to see different V_{zz} and $\rho_e(0)$ depending on the relative distance and orientation of nearby ^{229}Th doping sites. The nuclear transition frequency will be shifted positively or negatively depending on the orientation and position of surrounding defects. As the density of thorium increases, the microstrain from nearby thorium overlaps more, leading to the increased inhomogeneous broadening. This scenario has been described in theoretical[44] and experimental[45] nuclear quadrupole resonance studies of defect broadening in crystals, in which a linear dependence of linewidth on concentration is expected assuming randomly distributed point defects. The non-zero intercept of approximately 25 kHz may be attributed to the presence of known CaF_2 crystal defects not connected with ^{229}Th.

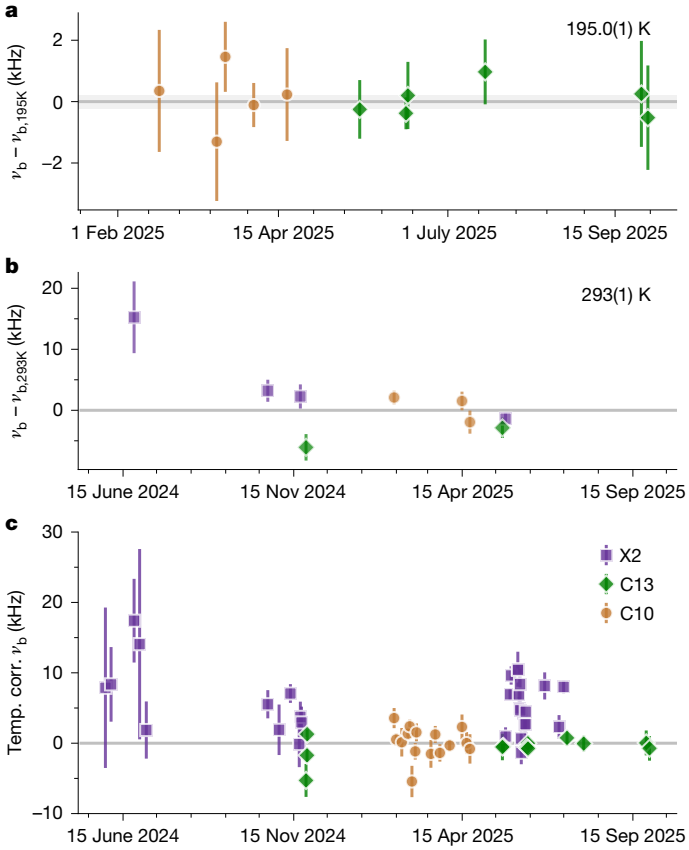

Fig. 4 | Time record of the line b nuclear transition frequency across all three crystals. Error bars from the Lorentzian fit are shown. **a**, Frequency ν_b at 195.0(1) K, near the zero-shift temperature T_0, over a 7-month period, relative to the average frequency of line b at 195 K. The standard error, shown with light grey shading, is 220 Hz. **b**, Frequency ν_b of line b at 293(1) K over a 1-year period, relative to the average frequency of line b at 293 K. **c**, Time dependent residuals of frequency ν_b from the quadratic fit, representing temperature correction (temp. corr.). By subtracting the temperature-induced shifts, all of our historical line b data are organized together. No systematic drift of the nuclear clock frequency, calibrated against the ^{87}Sr optical clock, is observed. Some overlapping data points have been offset by a maximum of 4 days for clarity. Error bars include the uncertainty propagated from the temperature correction.

The observation that line c is always broader than line b may be similarly understood. The temperature dependence shown in Fig. 3 can be interpreted as a rough proxy for stress sensitivity, as increasing the crystal temperature or adding microstrain both distort the lattice, changing the electron density and electric field gradients. As ν_c changes more with temperature than ν_b, the inhomogeneous broadening should be greater for line c than line b in the same defect concentration environment. At this high spectral resolution, we still lack a quantitative theory connecting our observed linewidths to the microscopic defect environment, which could guide the design of other crystal hosts.

Experimentally we find that Lorentzian fits consistently yield smaller residuals than Gaussian lineshape fits (see Extended Data Fig. 1 for an example). Based on earlier work in nuclear magnetic resonance and Mössbauer spectroscopy, a Lorentzian lineshape is expected for transitions dominated by electric field gradient effects in low concentration point-defect-broadened crystals[44,46]. For a Poissonian defect distribution and for the frequency shift due to microstrain falling off as inverse of cubic distance, the resulting lineshape is Lorentzian[47].

The microstrain-related broadening mechanism can be investigated further in several ways. Crystals doped with both ^{229}Th and ^{232}Th could allow exploration of different defect concentration environments, as ^{232}Th is expected to create the same defect sites as ^{229}Th but does not possess the 148 nm nuclear transition. With sufficient laser intensity, spectral hole-burning or spin-echo experiments can also be used to confirm the inhomogeneous broadening mechanism.

Techniques such as X-ray diffraction or atomic force microscopy can give insight to the crystalline structure, as has been done for ^{232}Th:CaF_2 (refs. 48,49). X-ray absorption fine structure spectroscopy has provided better understanding of the defect structure and interstitial positions for ^{229}Th:CaF_2 (ref. 50), which could be used to form theoretical models of the strain defect. Finally, we note that crystals in which thorium is naturally part of the crystal lattice rather than a defect, demonstrated by early experimental work in ThF_4 (ref. 51) or theoretically in $Th(SO_4)_2$ (ref. 52), should be free from this microstrain effect. In this case, other defects intrinsic to the host material or due to ^{229}Th radioactivity may dominate. With anticipated further increases of the spectral resolution for laser-driven nuclear transition, the study of linewidth and absolute transition frequency will become an increasingly sensitive probe of material properties.

Other systematics and outlook

To build a practical nuclear clock, several other important systematic effects must be investigated. The interaction of the nuclear magnetic moment μ_I and a magnetic field B results in the splitting of $\pm m$ levels, also known as the nuclear Zeeman effect. The shift of each level is given by $\mu_I mB$, corresponding to roughly 1 kHz G^{-1} depending on the specific transition and orientation of B with respect to the EFG. The stray magnetic field in our current experiment, estimated to be <1 G, would not cause a noticeable effect in the ^{229}Th:CaF_2 crystals, but this may become important for future crystals with less inhomogeneous broadening. Moreover, the intensity and frequency of the Zeeman split lines can yield insight into the intrinsic magnetic environment[53]. By changing the magnetic field orientation, the EFG tensor within the crystal can also be characterized[54]. Another interesting investigation would be to subject the crystal to different stresses and measure potential frequency shifts as the electron density and EFG changes, which may clarify the observed X2 frequency scatter.

The fractional frequency stability of a clock is characterized by $\sigma \propto \frac{\Delta f}{f_0 S}\sqrt{T_{cycle}/\tau}$. Based on the current experimental conditions achieved for the C10 crystal, the linewidth $\Delta f = 30$ kHz, centre frequency $f_0 = 2{,}020.407$ THz, cycle time $T_{cycle} = 600$ s, signal-to-noise ratio $S = 20$ over T_{cycle} and τ the averaging time[13], we expect $\sigma \approx 10^{-11}/\sqrt{\tau}$. Although far below the performance of atomic clocks of present day, this can be used as a guideline for future nuclear clock development, namely, by improving Δf, S and T_{cycle}.

As previously discussed, in a crystal free of inhomogeneous microstrain broadening the linewidth may be reduced to the kHz level, improving σ by more than an order of magnitude. With a higher ^{229}Th doping concentration crystal or with a higher intensity excitation laser, the signal can be linearly improved. Suppressing the background counts by veto detection[32,55] or using a crystal with a lower intrinsic background also increases the signal-to-noise ratio S.

A huge gain can be achieved by reducing T_{cycle}, which currently consists of 400 s of laser irradiation and 200 s of fluorescence photon detection. This could be obtained by using a higher-power laser and improved readout techniques. The Rabi frequency for our current laser is estimated to be approximately 0.1 Hz, much smaller than the observed linewidth of 30 kHz. To enable coherent control of the nuclear population, the Rabi frequency should be of the order of the inhomogeneous linewidth or greater, which requires a substantial laser power upgrade or linewidth reduction. With a single-frequency continuous-wave laser rather than a frequency comb, the excited state could be read out through absorption instead of nuclear decay, potentially allowing continuous clock operation.

The coupling of electronic and nuclear states within the crystal could also be harnessed to control the nuclear population. A laser-induced

quenching effect has been observed for doped ^{229}Th crystals, in which shining off-resonant 200–400 nm light reduced the excited state lifetime by up to a factor of 3 (refs. 35,56). A similar quenching effect was first reported with 29 keV X-ray beams used to indirectly excite the nuclear transition[32,57]. If these effects could yield higher signal over a shorter collection time, it would help improve σ. Similarly, if a nuclear state-dependent electronic transition exists in the crystal, it could be used to quickly readout the clock state with higher S than the current fluorescence detection. Improved theoretical models for the microscopic defect structure in the crystal will be crucial for understanding these effects as well as the observed temperature-dependent frequency shifts in this work.

An important application of the nuclear clock to fundamental physics is constraining variations of fundamental constants, which are proposed in many ultralight dark matter (ULDM) models. The nuclear clock has orders of magnitude enhanced sensitivity to this effect compared with atomic clocks because the ULDM couples dominantly to the nucleus (quantum chromodynamic sector)[6–8,58]. An analysis[8] shows that a ^{229}Th nuclear clock with frequency uncertainty of 5 kHz can already begin to put competitive bounds on the ULDM mass and coupling strength. The lineshape may also be of interest for constraining high-frequency temporal variations. Using the strontium atomic clock as a reference, our current and future time record of the nuclear transition frequency can sensitively probe ULDM.

In summary, we report quantum-state-resolved nuclear spectroscopy on three separately grown ^{229}Th:CaF_2 crystals and verify the frequency reproducibility of the ^{229}Th nuclear transition over a 1-year period. Taking detailed temperature dependence data for line b ($m = \pm5/2 \rightarrow m = \pm3/2$), we identify a temperature $T = 196(5)$ K, at which the first-order temperature dependence of ν_b vanishes. At this temperature, we find the reproducibility of ν_b is 220 Hz across two different crystals over 7 months. By performing a co-thermometry scheme with a more temperature-sensitive transition such as line c, the systematic temperature shift could be suppressed below the 10^{-18} fractional uncertainty level. We also observe a linear dependence of the nuclear transition linewidth on ^{229}Th doping concentration, which sheds light on how the ^{229}Th dopant distorts the crystalline host. This work shows the reliability of ^{229}Th:CaF_2 crystals as a frequency reference and the first characterization of crystal-limited linewidths, representing an important step towards field-deployable solid-state nuclear clocks.

Online content

Any methods, additional references, Nature Portfolio reporting summaries, source data, extended data, supplementary information, acknowledgements, peer review information; details of author contributions and competing interests; and statements of data and code availability are available at https://doi.org/10.1038/s41586-025-09999-5.

1. Tiedau, J. et al. Laser excitation of the Th-229 nucleus. *Phys. Rev. Lett.* **132**, 182501 (2024).
2. Elwell, R. et al. Laser excitation of the ^{229}Th nuclear isomeric transition in a solid-state host. *Phys. Rev. Lett.* **133**, 013201 (2024).
3. Zhang, C. et al. Frequency ratio of the ^{229m}Th nuclear isomeric transition and the ^{87}Sr atomic clock. *Nature* **633**, 63–70 (2024).
4. Zhang, C. et al. $^{229}ThF_4$ thin films for solid-state nuclear clocks. *Nature* **636**, 603–608 (2024).
5. Beeks, K. et al. The thorium-229 low-energy isomer and the nuclear clock. *Nat. Rev. Phys.* **3**, 238–248 (2021).
6. Beeks, K. et al. Fine-structure constant sensitivity of the Th-229 nuclear clock transition. *Nat. Commun.* **16**, 9147 (2025).
7. Caputo, A. et al. Sensitivity of nuclear clocks to new physics. *Phys. Rev. C* **112**, L031302 (2025).
8. Fuchs, E. et al. Searching for dark matter with the ^{229}Th nuclear lineshape from laser spectroscopy. *Phys. Rev. X* **15**, 021055 (2025).
9. Kazakov, G. A. et al. Performance of a ^{229}Thorium solid-state nuclear clock. *New J. Phys.* **14**, 083019 (2012).
10. Aeppli, A., Kim, K., Warfield, W., Safronova, M. S. & Ye, J. Clock with 8×10^{-19} systematic uncertainty. *Phys. Rev. Lett.* **133**, 023401 (2024).
11. Higgins, J. S. et al. Temperature sensitivity of a thorium-229 solid-state nuclear clock. *Phys. Rev. Lett.* **134**, 113801 (2025).
12. Beeks, K. et al. Growth and characterization of thorium-doped calcium fluoride single crystals. *Sci. Rep.* **13**, 3897 (2023).
13. Ludlow, A. D., Boyd, M. M., Ye, J., Peik, E. & Schmidt, P. O. Optical atomic clocks. *Rev. Mod. Phys.* **87**, 637–701 (2015).
14. Marshall, M. C. et al. High-stability single-ion clock with 5.5×10^{-19} systematic uncertainty. *Phys. Rev. Lett.* **135**, 033201 (2025).
15. Bothwell, T. et al. Resolving the gravitational redshift across a millimetre-scale atomic sample. *Nature* **602**, 420–424 (2022).
16. Rellergert, W. G. et al. Constraining the evolution of the fundamental constants with a solid-state optical frequency reference based on the Th 229 nucleus. *Phys. Rev. Lett.* **104**, 200802 (2010).
17. Tkalya, E. V., Varlamov, V. O., Lomonosov, V. V. & Nikulin, S. A. Processes of the nuclear isomer ^{229m}Th (3/2$^+$, 3.5 ± 1.0 eV) resonant excitation by optical photons. *Phys. Scr.* **53**, 296 (1996).
18. Peik, E. & Tamm, C. Nuclear laser spectroscopy of the 3.5 eV transition in Th-229. *Europhys. Lett.* **61**, 181 (2003).
19. Peik, E. et al. Nuclear clocks for testing fundamental physics. *Quantum Sci. Technol.* **6**, 034002 (2021).
20. von der Wense, L. & Seiferle, B. The ^{229}Th isomer: prospects for a nuclear optical clock. *Eur. Phys. J. A* **56**, 277 (2020).
21. von der Wense, L. et al. Direct detection of the ^{229}Th nuclear clock transition. *Nature* **533**, 47–51 (2016).
22. Thielking, J. et al. Laser spectroscopic characterization of the nuclear-clock isomer ^{229m}Th. *Nature* **556**, 321–325 (2018).
23. Seiferle, B. et al. Energy of the ^{229}Th nuclear clock transition. *Nature* **573**, 243–246 (2019).
24. Masuda, T. et al. X-ray pumping of the ^{229}Th nuclear clock isomer. *Nature* **573**, 238–242 (2019).
25. Yamaguchi, A. et al. Energy of the ^{229}Th nuclear clock isomer determined by absolute γ-ray energy difference. *Phys. Rev. Lett.* **123**, 222501 (2019).
26. Sikorsky, T. et al. Measurement of the ^{229}Th isomer energy with a magnetic microcalorimeter. *Phys. Rev. Lett.* **125**, 142503 (2020).
27. Kraemer, S. et al. Observation of the radiative decay of the ^{229}Th nuclear clock isomer. *Nature* **617**, 706–710 (2023).
28. Zhang, C. et al. Tunable VUV frequency comb for ^{229m}Th nuclear spectroscopy. *Opt. Lett.* **47**, 5591 (2022).
29. Elwell, R. et al. Laser-based conversion electron Mössbauer spectroscopy of $^{229}ThO_2$. *Nature* **648**, 300–305 (2025).
30. Beeks, K. et al. Optical transmission enhancement of ionic crystals via superionic fluoride transfer: growing VUV-transparent radioactive crystals. *Phys. Rev. B* **109**, 094111 (2024).
31. Dessovic, P. et al. ^{229}Thorium-doped calcium fluoride for nuclear laser spectroscopy. *J. Phys. Condens. Matter* **26**, 105402 (2014).
32. Hiraki, T. et al. Controlling ^{229}Th isomeric state population in a VUV transparent crystal. *Nat. Commun.* **15**, 5536 (2024).
33. Nalikowski, K., Veryazov, V., Beeks, K., Schumm, T. & Krośnicki, M. Embedded cluster approach for accurate electronic structure calculations of ^{229}Th:CaF_2. *Phys. Rev. B* **111**, 115103 (2025).
34. Hiraki, T. et al. Laser Mössbauer spectroscopy of ^{229}Th. Preprint at https://arxiv.org/abs/2509.00041 (2025).
35. Schaden, F. et al. Laser-induced quenching of the Th-229 nuclear clock isomer in calcium fluoride. *Phys. Rev. Res.* **7**, L022036 (2025).
36. Mestechkin, M. M. Electric field gradient in cubic and other ionic crystals. *J. Phys. Condens. Matter* **7**, 611–623 (1995).
37. Dunlap, B. & Kalvius, G. in *Handbook on the Physics and Chemistry of the Actinides* (eds Freeman, A. J. & Lander, G. H.) Vol. 2, 331–434 (North-Holland, 1985).
38. Torumba, D., Parlinski, K., Rots, M. & Cottenier, S. Temperature dependence of the electric-field gradient in hcp-Cd from first principles. *Phys. Rev. B* **74**, 144304 (2006).
39. Haas, H. Temperature dependence of electric-field gradient in Zn and Cd: Replacing the $T^{3/2}$ law. *Phys. Rev. B* **109**, 064104 (2024).
40. Shrivastava, K. N. Temperature dependence of the Mössbauer isomer shift. *Hyperfine Interact.* **26**, 817–843 (1985).
41. Oelker, E. et al. Demonstration of 4.8×10^{-17} stability at 1s for two independent optical clocks. *Nat. Photon.* **13**, 714–719 (2019).
42. Milner, W. R. et al. Demonstration of a timescale based on a stable optical carrier. *Phys. Rev. Lett.* **123**, 173201 (2019).
43. Eshelby, J. D. in *Solid State Physics* (eds Seitz, F. & Turnbull, D.) Vol. 3, 79–144 (Academic Press, 1956).
44. Stoneham, A. M. Shapes of inhomogeneously broadened resonance lines in solids. *Rev. Mod. Phys.* **41**, 82–108 (1969).
45. Pelzl, J., Vargas, H., Dautreppe, D. & Schulz, H. Influence of point defects on the nuclear quadrupole resonance of ^{35}Cl in $KClO_3$ and $NaClO_3$. *J. Phys. Chem. Solids* **36**, 791–796 (1975).
46. Kanert, O., Kotzur, D. & Mehring, M. Influence of point defects and dislocations on the line shape of nuclear magnetic resonance signals. *Phys. Status Solidi B Basic Solid State Phys.* **36**, 291–300 (1969).
47. Cohen, M. H. & Reif, F. in *Solid State Physics* (eds Seitz, F. & Turnbull, D.), Vol. 5, 321–438 (Academic Press, 1957).
48. Gong, Q. et al. Structures and properties of high-concentration doped Th:CaF_2 single crystals for solid-state nuclear clock materials. *Inorg. Chem.* **63**, 3807–3814 (2024).
49. Beeks, K. *The Nuclear Excitation of Thorium-229 in the* CaF_2 *Environment: Development of a Crystalline Nuclear Clock*. PhD thesis, Technische Universität Wien, Vienna (2022).
50. Takatori, S. et al. Characterization of the thorium-229 defect structure in CaF_2 crystals. *New J. Phys.* **27**, 043024 (2025).
51. Pastor, R. C. & Arita, K. Preparation and crystal growth of ThF4. *Mater. Res. Bull.* **9**, 579–583 (1974).

52. Morgan, H. W. T. et al. A spinless crystal for a high-performance solid-state ^{229}Th nuclear clock. Preprint at https://arxiv.org/abs/2503.11374 (2025).
53. Reissner, M. in *Modern Mössbauer Spectroscopy: New Challenges Based on Cutting-Edge Techniques* (eds Yoshida, Y. & Langouche, G.), 381–444 (Springer, 2021).
54. Liechti, O. & Kind, R. NMR-NQR rotation patterns of single crystals with quadrupolar inhomogeneities. *J. Mag. Reson.* **85**, 480–491 (1989).
55. Hiraki, T. et al. Experimental apparatus for detection of radiative decay of ^{229}Th isomer from Th-doped CaF_2. *Hyperfine Interact.* **245**, 14 (2024).
56. Terhune, J. E. S. et al. Photoinduced quenching of the ^{229}Th isomer in a solid-state host. *Phys. Rev. Res.* **7**, L022062 (2025).
57. Guan, M. et al. X-ray-induced quenching of the ^{229}Th clock isomer in CaF_2. Preprint at https://arxiv.org/abs/2505.03852 (2025).
58. Flambaum, V. V. Enhanced effect of temporal variation of the fine structure constant and the strong interaction in ^{229}Th. *Phys. Rev. Lett.* **97**, 092502 (2006).

Methods

Frequency comb and detection setup

The spectroscopic data were taken using a vacuum ultraviolet frequency comb generated by cavity-enhanced high harmonic generation (HHG). The details of this procedure are described in previous publications[28,59,60]. Briefly, we generate a high-power, near-infrared frequency comb with average power around 40 W and a repetition frequency of 75 MHz (IMRA America, centre wavelength about 1,040 nm). The comb is coupled to a femtosecond enhancement cavity for passive amplification of the comb power to 5 kW, achieving high enough pulse power for HHG in xenon gas. We outcouple the seventh harmonic from the cavity (centre frequency about 148 nm) and direct it onto the thorium-doped crystal.

The fundamental comb light is locked to the JILA strontium clock laser at 698 nm (ref. 10). This clock laser is locked to a Menlo frequency comb, which is stabilized to a cryogenic ultra-stable silicon cavity[41,61]. This allows for an absolute, frequency-based measurement of the thorium transition frequency. Furthermore, the fundamental comb is locked to a near-infrared non-planar ring oscillator at 1,064 nm, which itself is locked to the same Menlo comb. Locking the fundamental comb at two points in the optical domain surrounding the centre wavelength provides further stabilization that may narrow the VUV comb linewidth compared with previous works. Extended Data Fig. 2 summarizes this new locking scheme.

We note that in previous work, the frequency of the comb was swept about 100 kHz during the irradiation window for each point of the line scan, which may distort the fitted linewidth compared with later line scans, in which the laser frequency was kept fixed. However, the fitted line centre would not be distorted. Consequently, line scans with frequency sweeping are excluded from Fig. 2 but are included in Figs. 3 and 4.

Our photon detection scheme has been described previously[3]. We place the crystal into the focus of a parabolic mirror to collect photons radiated from the thorium nuclei. The light collimated from the parabolic mirror is spectrally filtered and imaged onto a photomultiplier tube (Hamamatsu). The line scans are conducted by stabilizing the carrier envelope offset frequency f_{CEO} of the fundamental comb to −8 MHz while scanning the repetition rate f_{rep}. Keeping the f_{CEO} constant facilitates the match of the fundamental comb with the modes of our enhancement cavity under its specific dispersion, which sets a preferred f_{CEO} for the highest efficiency harmonic generation. For each scan point, f_{rep} remains fixed while the crystal is irradiated for 400 s, followed by a 200 s detection window. For each transition, the comb mode number determination was done in previous work[3], allowing for a single scan of each lineshape for absolute frequency determination.

Data analysis

Each scan point signal is normalized by the average intensity of the excitation laser to reduce fluctuations from laser intensity drift. The excitation laser intensity is monitored using a camera capturing the visible fluorescence of the crystal under laser irradiation, similar to that presented in ref. 1. This fluorescence, which arises from self-trapped exciton emission[62], depends strongly on the laser power and not on laser frequency. In some scans, we observed the background count rate after the scan was higher than before the scan started, distorting the lineshape. This is corrected for by subtracting a linear baseline before other corrections.

The long excitation life of the nuclear transition also presents a 'memory' effect and may distort the measured line shape. In previous publications, this was mitigated by performing the frequency scan in forward and reverse directions[3]. Using the measured lifetime of the ^{229}Th transition in CaF_2 (refs. 1,3), we now remove this memory effect in post-processing of the data similar to that performed in ref. 1 so that a bidirectional scan is not needed and the intrinsic lineshape is clearly presented. For a typical scan, we first take two points far from resonance to establish the baseline counts B. The exponential decay from the ith detection window can then be fitted to $y_i(t) = A_i e^{-t/\tau} + B$, where A_i is the signal amplitude and $\tau = 641$ s is the measured nuclear excited state lifetime in seconds (ref. 3). The exponential decay from the previous detection window can be extrapolated to the current one and then subtracted out. The memory corrected detection window is $y_{i,\mathrm{corr}}(t) = y_i(t) - A_{i-1}e^{-(t+T)/\tau}$, where T is time since the beginning of the $i-1$ detection window.

For data taken over many months, a slight frequency shift from slow drift of the silicon cavity needs to be accounted for. By fitting a line to the silicon cavity (Si3) absolute frequency[42] measured against the JILA Sr1 atomic clock[10] from May 2024 to March 2025, a drift of −1.5 Hz per day is extracted. This corresponds to −15.6 Hz per day for the thorium transition frequency, which accumulates to more than 5 kHz over 12 months. The shift is calculated for each date and subtracted from each fitted frequency.

Discussions on linewidth

In the first report on high-resolution laser-based spectroscopy of the thorium nuclear clock transition[3], we recorded linewidths of around 300 kHz in the X2 crystal. For each data point in the line profiles, we swept the comb frequency over a 240 kHz range for the initial search and 100 kHz range for subsequent scans. At the time, we had no knowledge of the dominant broadening mechanism for the measured linewidth in this crystal. Only once we measured smaller linewidths in other crystals did we realize that the linewidths measured in ref. 3 were limited by a combination of crystal physics and the frequency sweeping technique. For this work, we thus made a few changes that affect the measured linewidth (in descending impact): keeping the laser frequency constant for each point of a line scan, the memory effect correction, and the changed locking scheme. In general, the reported linewidth represents the convolution of our laser linewidth and the crystal-limited nuclear transition linewidth. As stated in the main text, the linear relationship between doping concentration and linewidth suggests that the laser linewidth does not dominate our measurements. If the laser linewidth had a significant contribution, we may expect the slope of Fig. 2b to flatten at low concentration. Our estimates of the current VUV comb linewidth based on the residual frequency noise power spectral density within the stabilization servo loop[28] place it at the kHz level, which could be verified in the future with increasingly narrow linewidth crystals.

For the data shown in Fig. 2b, we explored if the different line b and c linewidths could be explained by the differences in angular momentum I in the electric quadrupole interaction Hamiltonian[37] $H_{E2} = \frac{QV_{zz}}{4I(2I-1)}[3I_z^2 - \mathbf{I}^2 + \eta(I_x^2 - I_y^2)]$. The transition energy of each line can be described as $E_i = V_{zz}A_i + E_{E1}$, where i = (b, c), $A_i = H_{E2}/V_{zz}$, and E_{E1} represents the electric monopole shift due to the local electron density $\rho_e(0)$. Assuming V_{zz} and E_{E1} do not depend on the line being excited, the A_i factor should capture the relationship between lines b and c. If the change in linewidth with doping concentration is solely due to differences in V_{zz}, then we expect that the ratio $A_c/A_b = m_c/m_b$, where m_i is the slope in Fig. 2b. In reality, $|A_c/A_b| = 0.7$, whereas $m_c/m_b = 1.8$. This difference shows that the relationship between ^{229}Th doping concentration and linewidth requires more advanced modelling to understand the underlying physics.

Quadrupole shift and temperature analysis

The frequency and temperature data shown in Fig. 3 is a combination of the electric monopole shift $\nu_{E1}(T)$ and electric quadrupole shift $\nu_{E2}(T)$ as a function of temperature T. The temperature dependence of the electric quadrupole splitting, which is proportional to the electric field gradient V_{zz}, often follows[38,63,64] the empirical relation $V_{zz}(T) = V_{zz}(0)(1 - BT^{\alpha})$, where $\alpha = 3/2$. Other values such as $\alpha = 1$ have also been observed[38]. This $T^{3/2}$ dependence can be reproduced by modelling the change in lattice vibrations with temperature, without considering any structural

(that is, lattice expansion) effects. More recent models[39] using modern density functional calculations of electronic structure can take both phonon and structural changes into account to accurately capture $V_{zz}(T)$. Calculations for the case of ^{229}Th:CaF_2, which will depend heavily on the exact charge compensation mechanism, will be explored in future work. In the following, we extract $\nu_{E2}(T)$ and show that in ^{229}Th:CaF_2 it follows $T^{3/2}$ dependence.

To isolate $\nu_{E2}(T)$ from $\nu_b(T) = \nu_{b,0} + \nu_{E1}(T) + \nu_{E2}(T)$, we use the 'unsplit frequency' data in Table 1 of ref. 11, which corresponds to the isomeric shift $\nu_{E1}(T)$. This unsplit frequency was obtained by taking a proper average of four quadrupole-split frequencies. Owing to the limited amount of data points, we use a linear fit to the data and obtain $y = -5.4(1)T + 1{,}600(30)$, where T is the temperature in kelvin and y is the unsplit frequency in kHz offset by 2,020,407,383,559 kHz. In our temperature range of 150–293 K, this linear approximation is reasonable[40,65,66]. We then subtract this from $\nu_b(T)$ to obtain the data points shown in Extended Data Fig. 3, in which the y-axis represents $\nu_{E2}(T)$ in kHz with an arbitrary frequency offset. Error bars include the uncertainty from Fig. 3 as well as the uncertainty from subtracting $\nu_{E1}(T)$.

We take $\nu_{E2}(T) \propto V_{zz}(T)$, using the approximation that the asymmetry parameter η is temperature independent. We then fit $\nu_{E2}(T) = \nu_0(1 - BT^{\alpha})$ to the data, with α fixed. For $\alpha = 3/2$, we obtain $\nu_0 = -1{,}328(4)$ kHz, and $B = 1.976(4) \times 10^{-4}\ \mathrm{K}^{-3/2}$ as shown in Extended Data Fig. 3 (top). Extended Data Fig. 3 (bottom) shows the residuals for $\alpha = 3/2$ as well as two more fits with $\alpha = 1$ and $\alpha = 2$. The residuals for $\alpha = 3/2$ show the least structure, suggesting that the EFG and temperature relation in ^{229}Th:CaF_2 follows $T^{3/2}$ in this temperature range.

Data availability

The datasets generated and analysed during this study are available at Zenodo[67] (https://doi.org/10.5281/zenodo.15751158).

59. Jones, R. J., Moll, K. D., Thorpe, M. J. & Ye, J. Phase-coherent frequency combs in the vacuum ultraviolet via high-harmonic generation inside a femtosecond enhancement cavity. *Phys. Rev. Lett.* **94**, 193201 (2005).
60. Gohle, C. et al. A frequency comb in the extreme ultraviolet. *Nature* **436**, 234–237 (2005).
61. Matei, D. G. et al. 1.5 μm lasers with sub-10 mHz linewidth. *Phys. Rev. Lett.* **118**, 263202 (2017).
62. Stellmer, S., Schreitl, M. & Schumm, T. Radioluminescence and photoluminescence of Th:CaF_2 crystals. *Sci. Rep.* **5**, 15580 (2015).
63. Christiansen, J. et al. Temperature dependence of the electric field gradient in noncubic metals. *Z. Phys. B Condens. Matter* **24**, 177–187 (1976).
64. Brown, R. J. C. Anomalous temperature dependence of NQR frequencies. *Z. Naturforsch. A* **45**, 449–458 (1990).
65. Shier, J. S. & Taylor, R. D. Temperature-dependent isomer shift and anharmonic binding of Sn 119 in Nb 3 Sn from Mössbauer-effect measurements. *Phys. Rev.* **174**, 346–350 (1968).
66. Coey, J. M. D., Sawatzky, G. A. & Morrish, A. H. Magnetization and temperature dependence of the Mössbauer spectrum shift for an insulator. *Phys. Rev.* **184**, 334–337 (1969).
67. Ooi, T. et al. Th-229 nuclear clock frequency record (JILA). *Zenodo* https://doi.org/10.5281/zenodo.15751158 (2025).

Acknowledgements We thank K. Kim, A. Aeppli, W. Warfield, D. Lee, B. Lewis and Z. Hu for running the Sr clock and ultrastable silicon cavity. We thank P. Li, K. Hagen, D. Warren, C. Schwadron, D. Reddy and K. Li for technical assistance and M. Ashton, B. C. Denton and M. R. Statham for help in dealing with radioactive samples. We acknowledge funding support from the National Science Foundation QLCI OMA-2016244, the DOE Quantum Center of Quantum System Accelerator, the Army Research Office (W911NF2010182), the Air Force Office of Scientific Research (FA9550-19-1-0148), DARPA (HR0011-25-3-0140), the National Science Foundation PHY-2317149 and the National Institute of Standards and Technology. Part of this work has been funded by the European Research Council (ERC) under the Horizon 2020 research and innovation programme of the European Union (grant agreement no. 856415) and the Austrian Science Fund (FWF) (grant DOIs 10.55776/F1004, 10.55776/J4834 and 10.55776/PIN9526523). The project 23FUN03 HIOC (grant DOI 10.13039/100019599) has received funding from the European Partnership on Metrology, co-financed by the Horizon Europe Research and Innovation Program of the European Union and by the participating states. We thank the National Isotope Development Center of DOE and the Oak Ridge National Laboratory for providing the ^{229}Th used in this work.

Author contributions T.O., J.F.D., C.Z., J.S.H. and J.Y. performed the experiment and analysed data; K.B., T. Sikorsky and T. Schumm grew the thorium-doped crystals and characterized its performance. All authors wrote the paper.

Competing interests The authors declare no competing interests.

Additional information
Supplementary information The online version contains supplementary material available at https://doi.org/10.1038/s41586-025-09999-5.

Correspondence and requests for materials should be addressed to Jun Ye.

Peer review information *Nature* thanks Sandro Kraemer and the other, anonymous, reviewer(s) for their contribution to the peer review of this work. Peer reviewer reports are available.

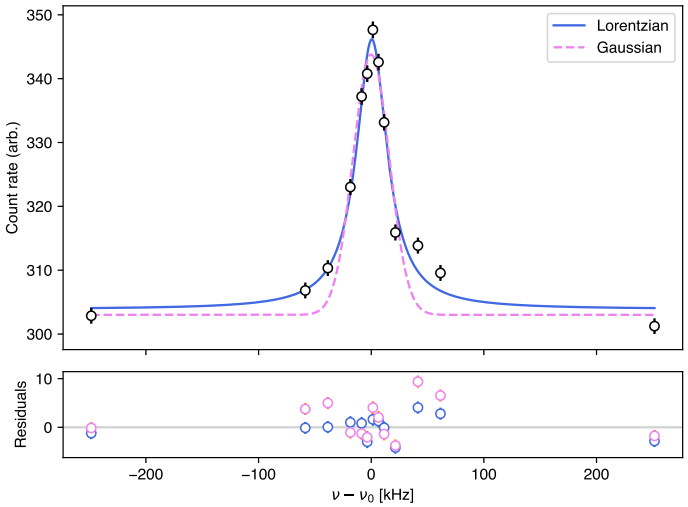

Extended Data Fig. 1 | Comparison of Gaussian versus Lorentzian fit for the example line scan shown in the inset of Fig. 2a, corresponding to line b of crystal C10 at 175 K. The Lorentzian fit center frequency is $\nu_0 = 2,020,407,298,706.6(8)$ kHz while the Gaussian fit center frequency is $\nu_{0,g} = 2,020,407,298,706(1)$ kHz. Fit residuals are shown on the lower panel, with error bars smaller than the markers. We find that a Lorentzian fit consistently yields smaller residuals compared to a Gaussian fit.

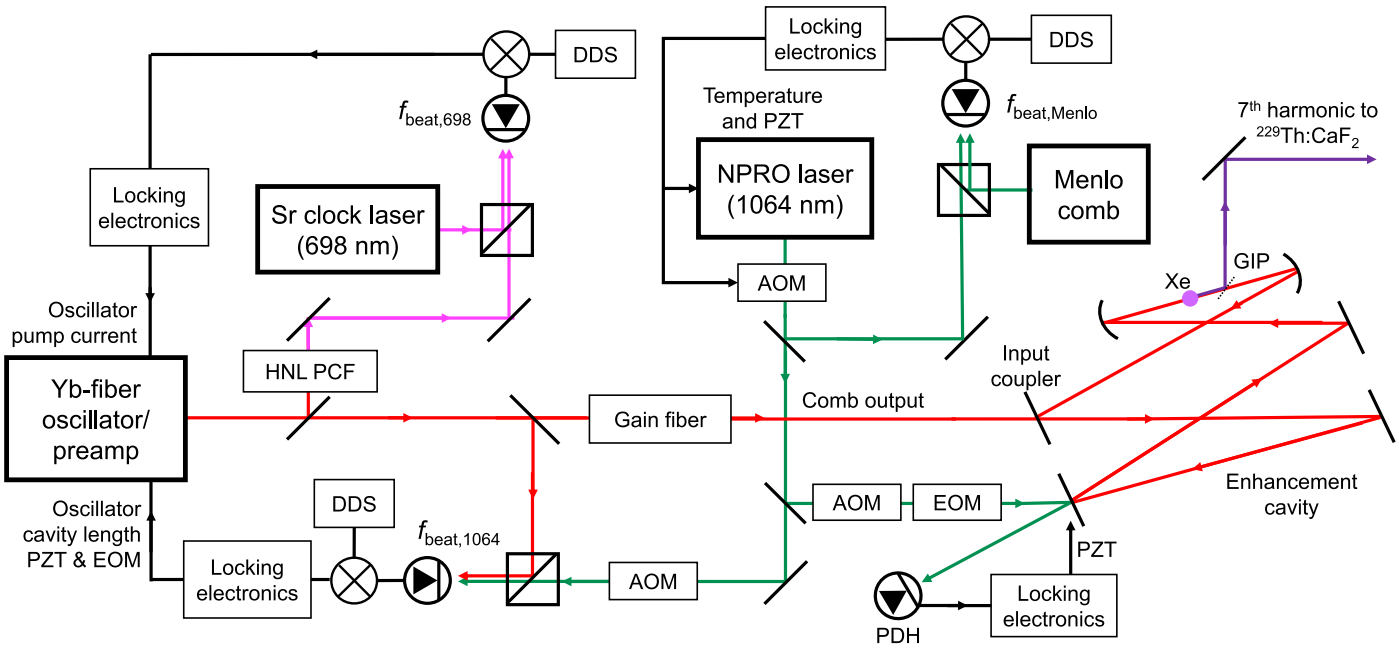

Extended Data Fig. 2 | Frequency comb locking scheme for data taken after September 15, 2024. A Yb-fiber oscillator from IMRA America generates the IR frequency comb centered around 1040 nm, which is coupled into our enhancement cavity for VUV harmonic generation. The IR frequency comb is locked at two points, which are scanned to adjust the repetition rate f_{rep} while keeping the carrier envelope offset $f_{CEO} = -8$ MHz. For the first point, 698 nm comb light generated from a highly nonlinear photonic crystal fiber (HNL PCF) beats with the Sr clock laser, indicated by $f_{beat,698}$. The desired beat frequency is set by a direct digital synthesizer (DDS), and the error signal feeds back onto the oscillator pump current. For the second point, 1064 nm comb light beats with a non-planar ring oscillator (NPRO) Mephisto laser, indicated by $f_{beat,1064}$. The error signal feeds back onto the oscillator cavity length and electro-optic modulator (EOM). The NPRO laser itself is stabilized to the Menlo comb, indicated by $f_{beat,Menlo}$, which feeds back onto the NPRO cavity length (PZT, piezo-electric transducer), temperature, and an acousto-optic modulator (AOM). The Sr clock laser is locked to the Menlo comb, and the Menlo comb is locked to the ultrastable silicon cavity (not shown). This scheme is designed to give the comb more robustness and frequency stability. NPRO light is used to stabilize the enhancement cavity using a Pound-Drever-Hall lock, with feedback onto one of the enhancement cavity mirrors.

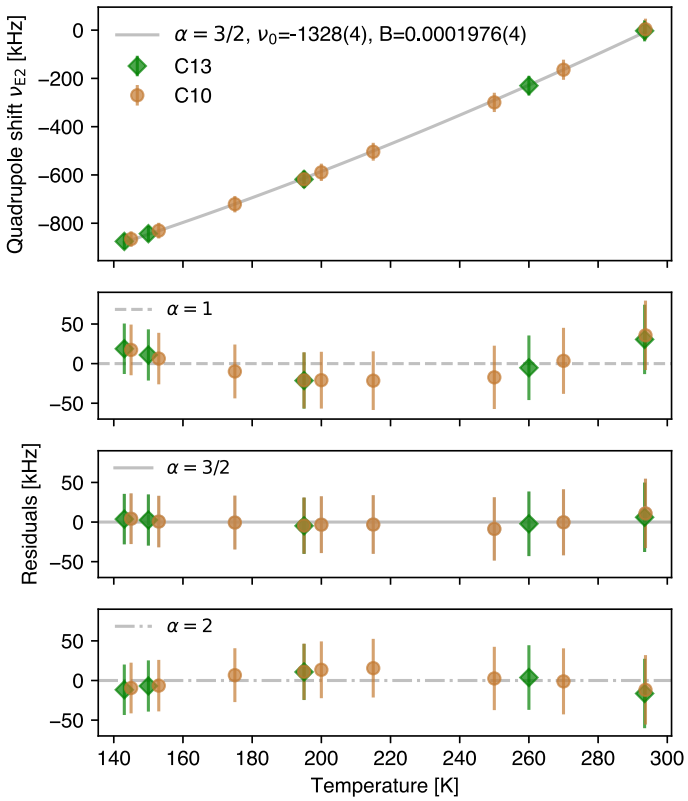

Extended Data Fig. 3 | Quadrupole (E2) shift versus temperature fit to the phenomenological formula $\nu_{E2}(T) = \nu_0(1 - BT^{\alpha})$. Top panel: data points for peak b in C10 and C13 show the quadrupole shift $\nu_{E2}(T)$ (in kHz, with an arbitrary frequency offset) plotted against temperature in Kelvin. The fit shown has $\alpha = 3/2$ fixed, with fitted parameters $\nu_0 = -1328(4)$ kHz and $B = 1.976(4) \times 10^{-4}$ K$^{-3/2}$. Lower panels: residuals for the $\alpha = 3/2$ fit shown in the top panel, as well as residuals for two other fits where $\alpha = 1$ and $\alpha = 2$ were fixed and ν_0, B were floated. The error bars shown include the error propagated from the isomeric shift subtraction. The residuals of $\alpha = 3/2$ show the least structure, which suggests the $T^{3/2}$ behavior observed in other materials.

Extended Data Table 1 | Quadratic fit parameters for center frequency v versus temperature T, where $v = \alpha T^2 + \beta T + \gamma$

	line b	line c
α [kHz/K^2]	0.0088(2)	-0.0137(9)
β [kHz/K]	-3.45(7)	-10.4(4)
γ [kHz]	255(7)	4220(40)